Supporting Information for "*Anisotropic Interlayer Force Field for Group-VI Transition Metal Dichalcogenides*"

Wenwu Jiang,[1#] Reut Sofer,[2#] Xiang Gao,[2#] Alexandre Tkatchenko,[3] Leeor Kronik,[4]
Wengen Ouyang,[1,5*] Michael Urbakh,[2*] and Oded Hod[2]

[1]*Department of Engineering Mechanics, School of Civil Engineering, Wuhan University, Wuhan, Hubei 430072, China*

[2]*School of Chemistry and The Sackler Center for Computational Molecular and Materials Science, Tel Aviv University, Tel Aviv 6997801, Israel*

[3]*Department of Physics and Materials Science, University of Luxembourg, L-1511 Luxembourg City, Luxembourg*

[4]*Department of Molecular Chemistry and Materials Science, Weizmann Institute of Science, Rehovoth 76100, Israel*

[5]*State Key Laboratory of Water Resources and Hydropower Engineering Science, Wuhan University, Wuhan 430072, China*

#: These authors contribute equally to this work.

[*]Corresponding authors. Email: w.g.ouyang@whu.edu.cn, urbakh@tauex.tau.ac.il

This supporting information document includes the following sections:

1. Convergence Tests of the Reference DFT Calculations

Generally speaking, the convergence of the DFT reference results depends on the choice of basis-set, reciprocal-space *k*-grid density, and vacuum size. In our previous interlayer potential (ILP) parameterization for MoS_2,[1] we found that the tier-2 basis-set yields well converged binding energies (BEs). Therefore, we adopt this basis set also in the present study and check for BE convergence with respect to the *k*-grid density and vacuum size used in the calculations of the studied bilayer systems. **Figure S1** and **Figure S2** present the convergence of the BEs of AA stacked $MoSe_2$ and WSe_2 bilayers with respect to the *k*-grid density and vacuum size, respectively. In each graph only one parameter is varied, and the rest are kept the same as detailed in the main text. Red symbols mark the parameter values employed to generate the reference results used in the main text. It is seen that the choice of *k*-grid of 19×19×1 and vacuum size of 100 Å provides BE convergence to within ~0.05 meV/atom, which is satisfactory for the purposes of the present study.

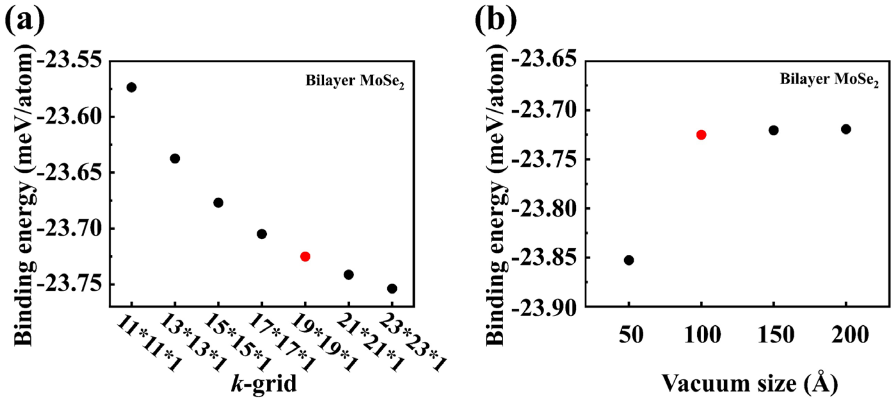

Figure S1. BE convergence tests for bilayer AA'-stacked $MoSe_2$ with respect to (a) the *k*-grid density and (b) the unit-cell vacuum size. The red-colored symbols mark the values used to obtain the results presented in the main text. The vacuum size used to obtain the results in panel a was fixed at 100 Å and the *k*-grid used to obtain the results presented in panel b was chosen to be 19×19×1. The interlayer distances in both panels were fixed at 6.6 Å.

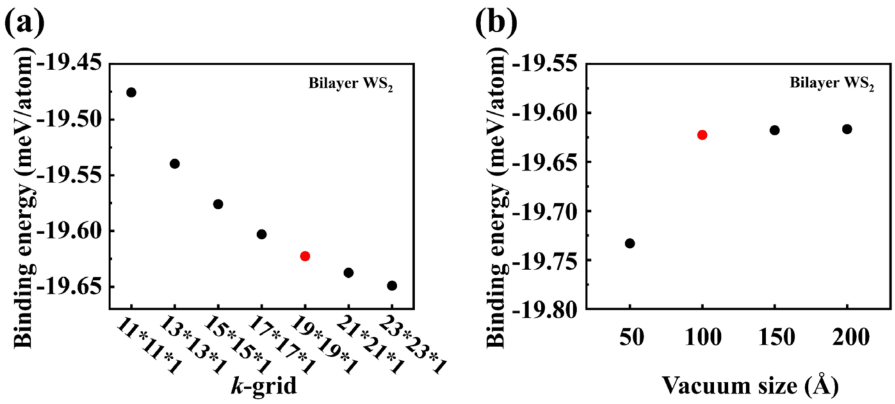

Figure S2. BE convergence tests for bilayer AA'-stacked WS_2 with respect to (a) the *k*-grid density and (b) the unit-cell vacuum size. The red colored symbols mark the values used to obtain the results presented in the main text. The vacuum size used to obtain the results in panel a was fixed at 100 Å and the *k*-grid used to obtain the results presented in panel b was chosen to be 19×19×1. The interlayer distances in both panels were fixed at 6.3 Å.

2. Additional Sliding Potential Energy Surfaces

In the main text, we provided sliding potential energy surfaces (PESs) for representative TMD bilayers. In this section, we provide PESs for the remaining two homojunctions (**Figure S3**: bilayer WS_2 and **Figure S4**: bilayer WSe_2) and one heterojunction (**Figure S5**: bilayer $MoS_2/MoSe_2$), which are included in the registry-dependent ILP parameterization training set. For each bilayer system, the reference DFT results (left columns), the ILP surfaces (middle columns), and their differences (right columns) are presented for the parallel (top panels) and anti-parallel (bottom panels) stacking modes. Overall, the ILP predications fit well with the DFT reference data with minor deviations of the order of ~1 meV/atom.

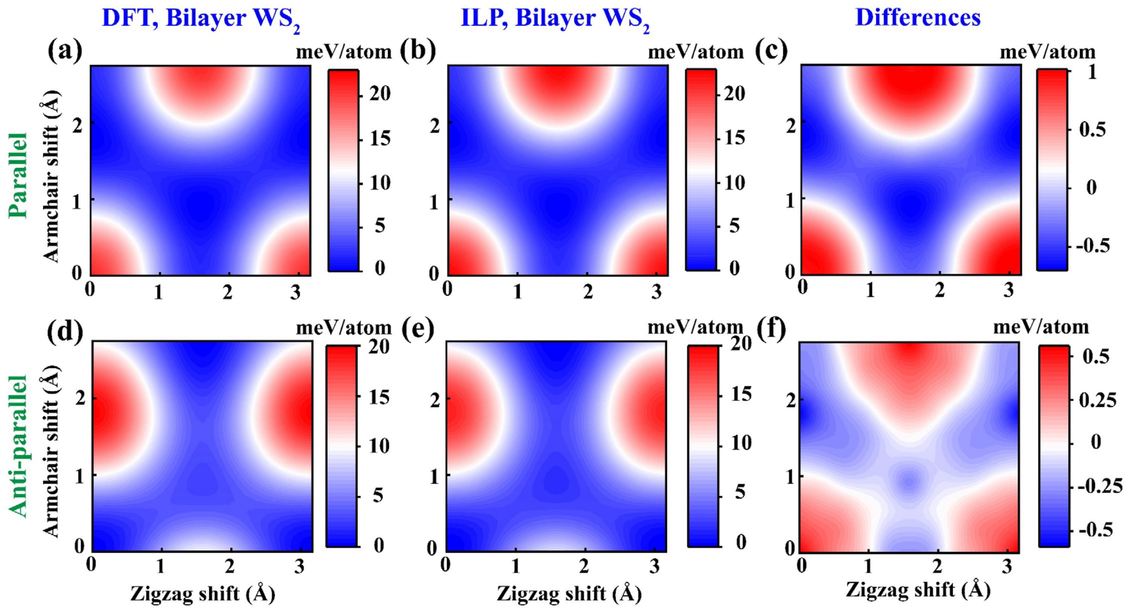

Figure S3. Sliding energy surfaces of the homogeneous WS_2 bilayer, calculated at an interlayer distance of 6.3 Å for the parallel (top panels) and antiparallel (bottom panels) configurations. The left and middle columns present the DFT (HSE+MBD-NL) and ILP PESs, and the right column presents their difference maps. The parameters presented in **Table S1** in the SI are used for the ILP calculations. The reported energies are normalized by the total number of atoms in the unit-cell (6 atoms) and measured relative to the values obtained at the AA' and AB stacking modes for the anti-parallel and parallel configurations, respectively.

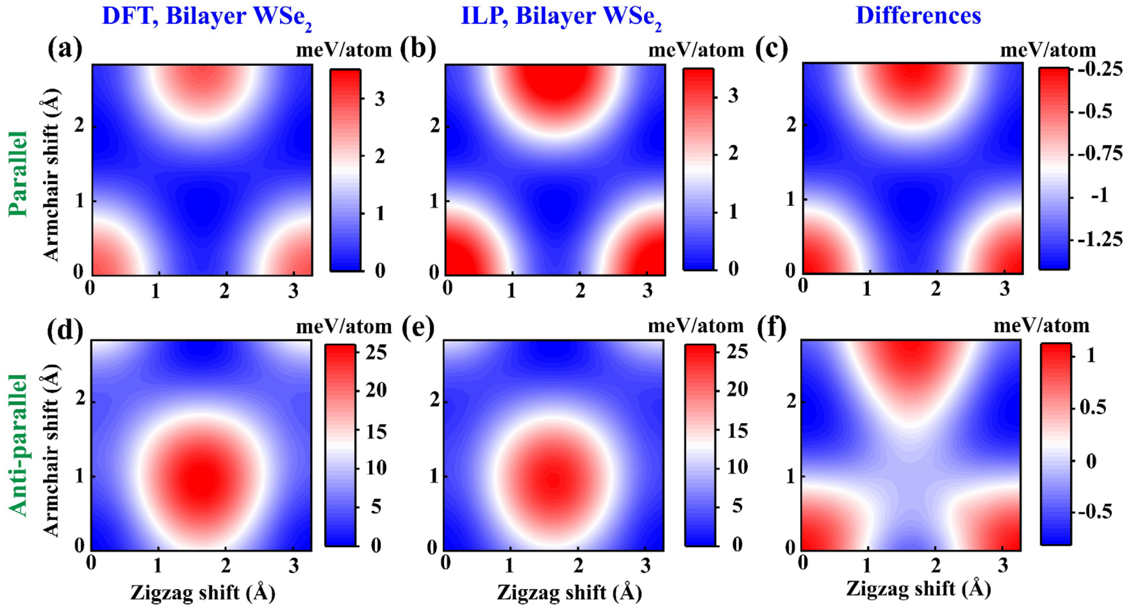

Figure S4. Sliding energy surfaces of the homogeneous WSe_2 bilayer, calculated at an interlayer distance of 7.3 Å for the parallel (top panels) and 6.6 Å for the antiparallel (bottom panels) configurations. The left and middle columns present the DFT (HSE+MBD-NL) and ILP PESs, and the right column presents their difference maps. The parameters presented in **Table S1** in the SI are used for the ILP calculations. The reported energies are normalized by the total number of atoms in the unit-cell (6 atoms) and measured relative to the values obtained at the AA' and AB stacking modes for the anti-parallel and parallel configurations, respectively.

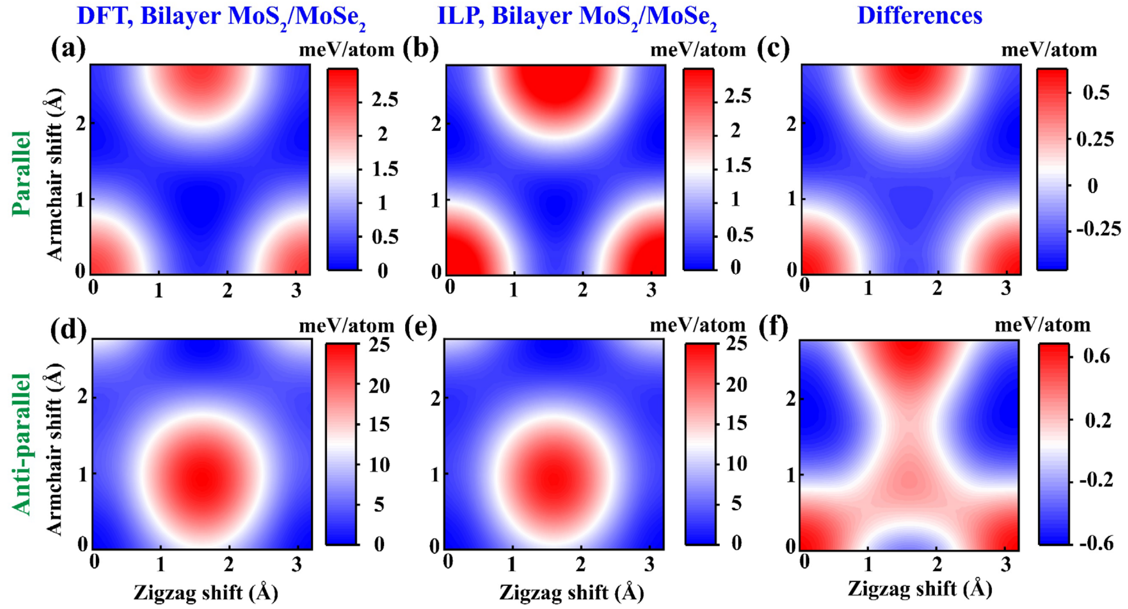

Figure S5. Sliding energy surfaces of the heterogeneous MoS$_2$/MoSe$_2$ bilayer, calculated at an interlayer distance of 7.1 Å for the parallel (top panels) and 6.4 Å for the antiparallel (bottom panels) configurations. The left and middle columns present the DFT (HSE+MBD-NL) and ILP PESs, and the right column presents their difference maps. The parameters presented in **Table S1** in the SI are used for the ILP calculations. The reported energies are normalized by the total number of atoms in the unit-cell (6 atoms) and measured relative to the values obtained at the AA' and AB stacking modes for the anti-parallel and parallel configurations, respectively.

3. Interlayer Potential Parameters

The ILP parameter values obtained by the fitting procedure described in the main text against DFT reference datasets at the level of HSE+MBD-NL for the various interfaces considered are presented in **Table S1**.

Table S1. List of ILP parameter values for laterally periodic bilayer MX_2 (M = Mo, W; X = S, Se). The training set includes all HSE+MBD-NL bilayer binding energy curves and sliding potential energy surfaces appearing in **Figures 2-4** of the main text and **Figure S3-Figure S5** in the SI. A value of $R_{\text{cut}} = 16$ Å is used throughout. Note that all parameters are symmetric with respect to indices interchange, e.g. $\alpha_{\text{Mo,S}} = \alpha_{\text{S,Mo}}$.

	β_{ij} (Å)	α_{ij}	γ_{ij} (Å)	ε_{ij} (meV)	C_{ij} (meV)	d_{ij}	$s_{R,ij}$	$r_{eff,ij}$ (Å)	$C_{6,ij}$ (eV·Å^6)
Mo-Mo	5.5795	9.3777	2.0272	144.1518	97.9786	89.4376	2.0590	5.1221	491.8503
W-W	5.5309	6.6250	1.9832	0.2718	140.1741	107.3926	1.3563	4.4376	691.8502
S-S	3.1614	8.0933	1.9531	4.5868	118.0655	58.8094	0.2154	4.2996	148.8112
Se-Se	3.9386	10.5159	2.4158	3.0126	22.4006	116.8645	0.1511	5.8842	112.5062
Mo-S	3.6272	19.9714	7.5850	76.1019	3.3175	45.7203	0.9475	4.4104	150.5979
Mo-Se	6.1964	4.8441	14.3620	7.4072	0.0588	27.1562	0.9768	3.9792	786.0298
W-S	3.6801	11.1630	32.2541	110.0197	79.3813	138.3404	0.9007	8.8758	250.6008
W-Se	3.9420	21.3275	0.0009	38.7174	49.6776	1.6196	2.5486	2.8992	654.2895
Mo-W	5.4123	8.6471	2.1087	51.1780	184.3429	201.2813	2.5477	2.4923	99.9969
S-Se	2.8201	7.4912	1.9333s	141.5326	293.1278	90.4709	0.3905	4.1709	117.6890

4. Importance of Coulomb Interactions

In the main text, we have demonstrated that the parameterized ILP, without explicit consideration of Coulomb interactions, reproduces well the binding energy curves and sliding potential energy surfaces of DFT reference data for polarizable TMD materials. This indicates that the contribution of interlayer Coulomb interactions to the binding physics should be rather weak. To confirm this, we evaluated the interlayer monopolar electrostatic interactions based on a partial-charge analysis of the different TMD atoms.

Consider, for example, bilayer MoS_2, where a Mulliken-charge DFT analysis, performed for the minimal unit cell at the HSE+MBD-NL level of theory, yields partial atomic charges of $+0.52e$ and $-0.26e$ for Mo and S atoms, respectively. These values can then be used within the Coulomb electrostatic energy term $E = k\frac{q_i q_j}{r}, (r < r_c)$, where $k = 14.399645\ \mathrm{eV} \cdot \mathrm{Å} \cdot \mathrm{C}^{-2}$ is the Coulomb constant, q_i and q_j are the effective charges of atoms i and j (residing in different layers), and $r_c = 16\ \mathrm{Å}$ is the cutoff. To this end, we construct a supercell consisting of a rectangular bilayer section, where each layer contains 4,900 Mo + 9,800 S atoms, within the LAMMPS package[2] and performed laterally periodic electrostatic calculations using the Ewald summation technique.

Figure S6 and **Figure S7** present the calculated ILP BE curves and sliding PESs,[1] respectively, for the MoS_2 bilayer compared to the Coulomb term contribution. Notably, the latter contribution is a mere ~0.7% and ~2% of the full values of the BE and sliding potential energy barrier, respectively. This supports our choice to neglect monopolar electrostatic contributions in the ILP expression, in order to increase computational efficiency.[3]

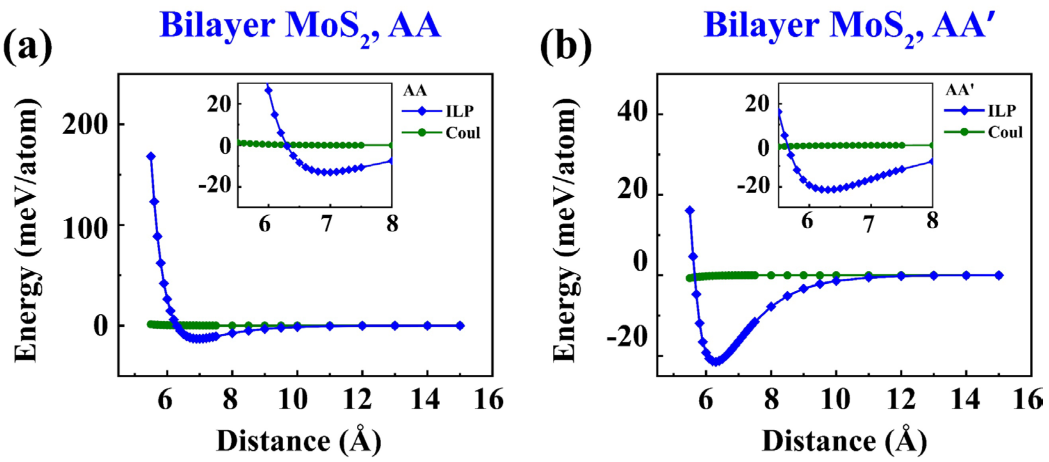

Figure S6. Binding energy curves of AA (a) and AA' (b) stacked MoS_2 bilayer calculated using the ILP (blue diamond) with the parameters of **Table S1**. The monopolar electrostatic term contribution is represented by the green circles. The reported energies are measured relative to the values of the two single layers (zero for the electrostatic term) and are normalized by the total number of atoms in the unit-cell (29,400 atoms). The insets provide a zoom-in on the equilibrium interlayer distance region.

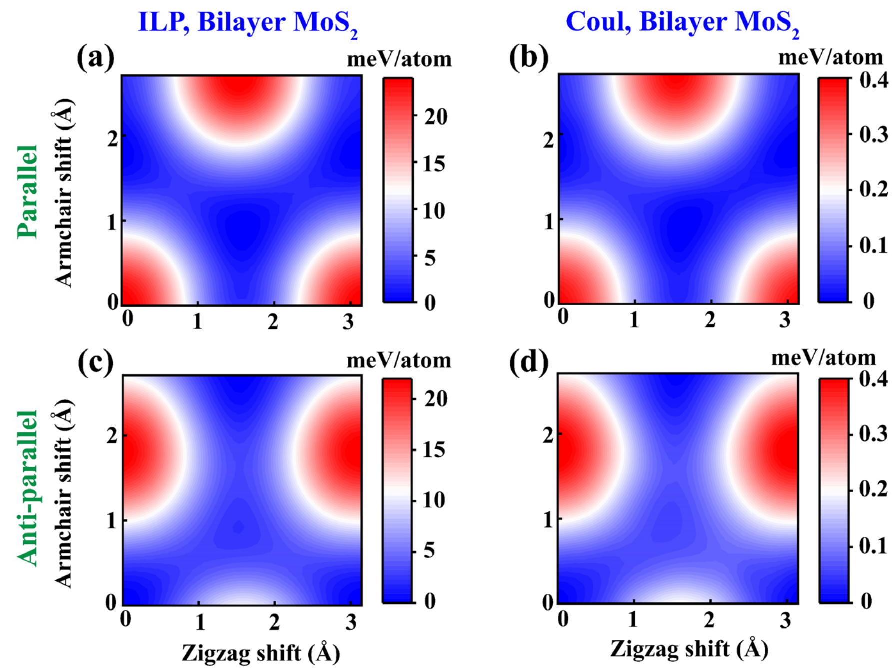

Figure S7. Sliding PESs of the bilayer MoS₂ homojunction, calculated at an interlayer distance of 6.24 Å for the parallel (top panels, starting from AA-stacking mode) and antiparallel (bottom panels, starting from AA′-stacking mode) configurations. ILP PESs obtained using the parameters presented in **Table S1** are presented in the left panels and the monopolar electrostatic contribution are presented in the right panels. The reported energies are normalized by the total number of atoms in the unit-cell (600 atoms) and measured relative to the values obtained at the AA' and AB stacking modes for the anti-parallel and parallel configurations, respectively.

5. Transferability of the developed ILPs

5.1 Binding Energy Curves

In this section, we demonstrate that the ILP parameterization presented in **Table S1** applies also to TMD heterojunctions that are outside the training set, as long as they contain the same atom types, which in our case, include the following AA' stacked heterojunctions: MoS_2/WSe_2, $MoSe_2/WS_2$, $MoSe_2/WSe_2$, and WS_2/WSe_2. In **Figure S8** we compare the ILP BE curves (red lines) against their DFT counterparts, calculated at the HSE+MBD-NL level of theory (black circles). The ILP BE curves compare well with the DFT calculations, with differences that are lower than ~2 meV/atom (10%) at the equilibrium separations of the different systems considered, thus demonstrating the transferability of the newly parameterized ILP.

We note that PBE+MBD-NL DFT calculations (bule triangle), which are less computationally cumbersome, provide a reasonable agreement with the HSE+MBD-NL values with differences lower than ~3 meV/atom (15%).

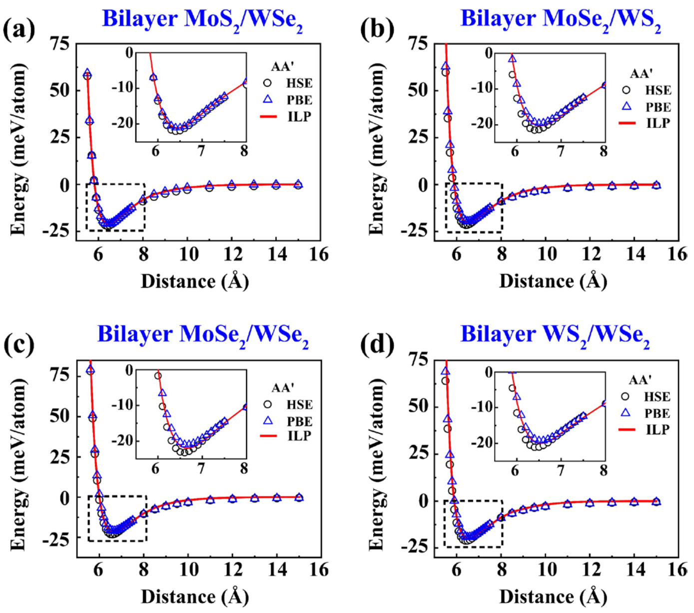

Figure S8. Binding energy curves for the four AA' stacked bilayer heterojunctions outside the ILP training set: (a) MoS_2/WSe_2, (b) $MoSe_2/WS_2$, (c) $MoSe_2/WSe_2$, and (d) WS_2/WSe_2 calculated using the newly parameterized (**Table S1**) ILP (red lines), and the HSE+MBD-NL (black circles) and PBE+MBD-NL (blue triangles) levels of DFT. The reported energies are measured relative to the values of the two single layers and are normalized by the total number of atoms in the unit-cell (6 atoms). The insets provide a zoom-in on the equilibrium interlayer distance region, marked by dashed black rectangles.

5.2 Sliding Potential Energy Surfaces

In addition to BE curves, we extended our analysis to include sliding PESs of three parallelly stacked bilayers that lie outside the ILP training set, namely $MoSe_2$ (**Figure S9**), WSe_2 (**Figure S10**), and MoS_2/WS_2 (**Figure S11**). The maximal difference we obtained between the DFT- and ILP-calculated PESs is of ~0.8 meV/atom (~3%), further demonstrating the remarkable accuracy of the ILP even when treating interface stacking configurations that were not originally included in the reference dataset.

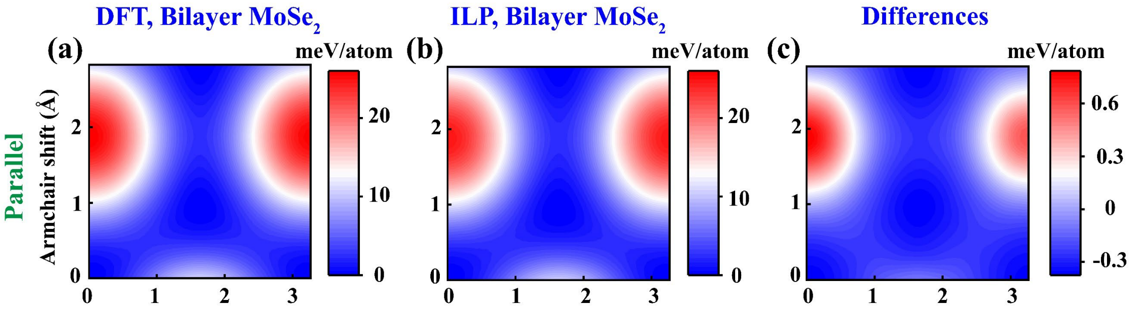

Figure S9. Sliding PESs of a parallelly-stacked $MoSe_2$ bilayer, calculated via rigid interlayer shifts at an interlayer distance of 6.6 Å (see Sec. 2.1 of the main text for computational details). The left and middle columns present the DFT (HSE+MBD-NL) and ILP PESs, and the right column presents their difference map. The parameters presented in **Table S1** above are used for the ILP calculations. The reported energies are normalized by the total number of atoms in the unit-cell (6 atoms) and measured relative to the values obtained at the AB stacking mode of the parallel configuration.

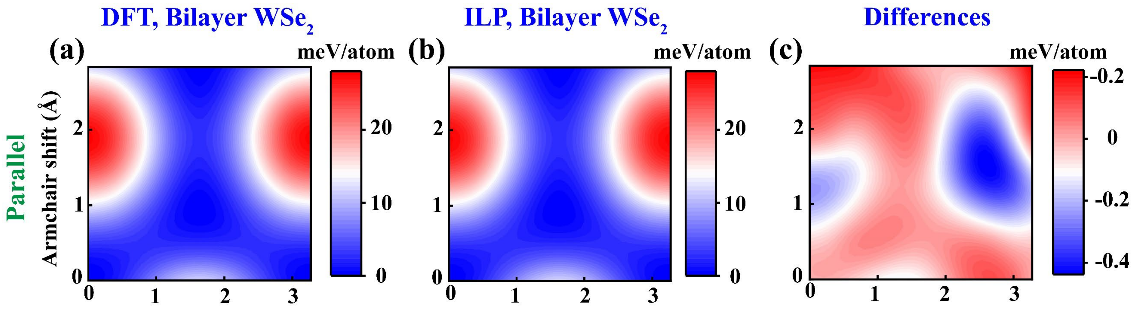

Figure S10. Sliding PESs of a parallelly-stacked WSe_2 bilayer, calculated via rigid interlayer shifts at an interlayer distance of 6.6 Å (see Sec. 2.1 of the main text for computational details). The left and middle columns present the DFT (HSE+MBD-NL) and ILP PESs, and the right column presents their difference map. The parameters presented in **Table S1** above are used for the ILP calculations. The reported energies are normalized by the total number of atoms in the unit-cell (6 atoms) and measured relative to the values obtained at the AB stacking mode of the parallel configuration.

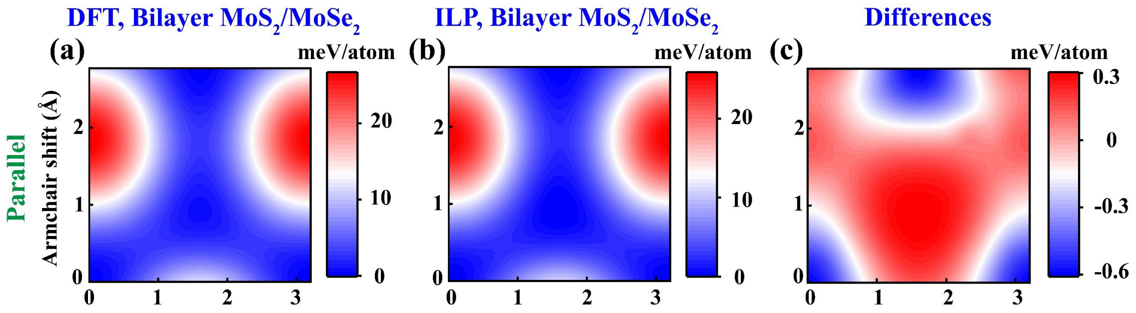

Figure S11. Sliding PESs of a parallelly-stacked $MoS_2/MoSe_2$ heterogeneous bilayer interface, calculated via rigid interlayer shifts at an interlayer distance of 6.4 Å (see Sec. 2.1 of the main text for computational details). The left and middle columns present the DFT (HSE+MBD-NL) and ILP PESs, and the right column presents their difference map. The parameters presented in **Table S1** above are used for the ILP calculations. The reported energies are normalized by the total number of atoms in the unit-cell (6 atoms) and measured relative to the values obtained at the AB stacking mode of the parallel configuration.

6. Bulk Moduli Fitting

The ILP pressure-volume (*P*-*V*) curves, used to evaluate the bulk moduli values reported in the main text, are presented in **Figure S12**. The evaluation is performed by fitting the ILP results with the Murnaghan equation (Eq. 8 of the main text, full blue lines),[4, 5] and two other equations of state (EOS): (i) The Birch-Murnaghan equation (Eq. S1, dashed red lines)[6, 7] and (ii) The Vinet equation (Eq. S2, dashed dotted purple lines),[8, 9] which take the following forms:

$$P = 3B_V^0\xi(1+2\xi)^{5/2}\left[1-\frac{3}{2}(4-B_V')\xi\right], \xi = \frac{1}{2}\left[\left(\frac{V}{V_0}\right)^{-\frac{2}{3}}-1\right] \tag{S1}$$

$$P = 3B_V^0\frac{(1-X)}{X^2}\exp\left[\frac{3}{2}(B_V'-1)(1-X)\right], X = \left(\frac{V}{V_0}\right)^{\frac{1}{3}} \tag{S2}$$

As in the Murnaghan equation, these two EOS also assume that B_V varies with pressure (hence the inclusion of the derivative B_V'). Nonetheless, they differ in their description of the dependence of B_V on the pressure, by assuming that it is linear, polynomial, and exponential for the Murnaghan, Birch–Murnaghan, and Vinet EOS, respectively.

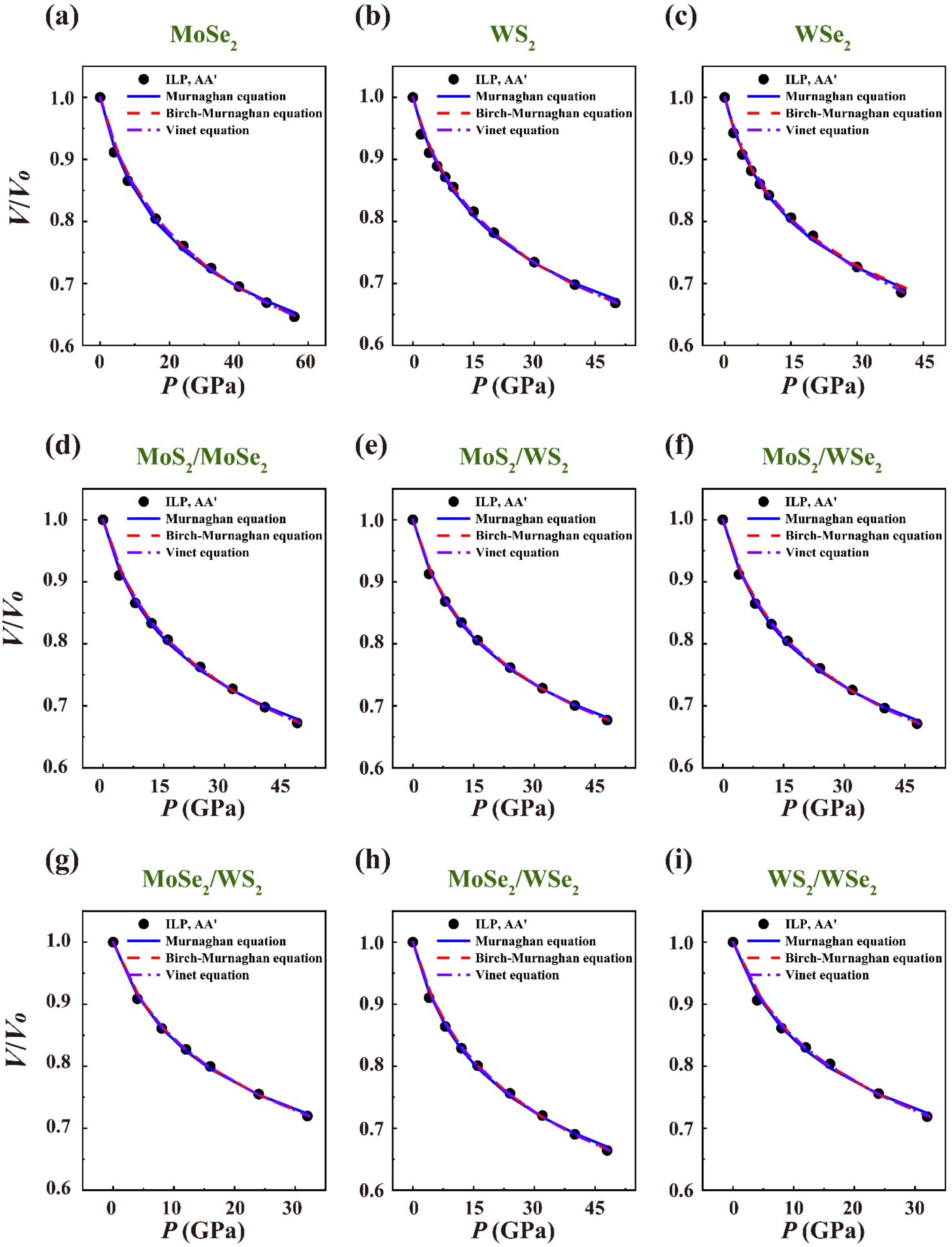

Figure S12. Pressure dependence of the normalized volume V/V_0 of nine homo- and heterojunctions. The solid black points are the NPT ILP simulations results. The solid blue, dashed red, and dashed-dotted purple lines are optimally-fitted curves obtained using Eq. 4 of the main text, Eq. S1, and Eq. S2, respectively.

The fitted bulk moduli (*B*) and its zero-pressure derivative (*B′*) for the six AA' stacked alternating heterojunctions considered are reported in **Table S2**.

Table S2. Bulk moduli, *B* (GPa), and their zero-pressure derivative, *B′* (GPa), of AA' stacked bulk $MoSe_2$, WS_2, and WSe_2, and alternating bulk heterojunctions of $MoS_2/MoSe_2$, MoS_2/WS_2, MoS_2/WSe_2, $MoSe_2/WS_2$, $MoSe_2/WSe_2$, WS_2/WSe_2.

Method/Material		$\mathbf{MoSe_2}$	$\mathbf{WS_2}$	$\mathbf{WSe_2}$
Murnaghan EOS	*B*	39.8 ± 5.8	38.6 ± 5.3	34.1 ± 4.1
	B′	4.8 ± 0.7	5.2 ± 0.8	5.5 ± 0.8
Birch−Murnaghan EOS	*B*	43.7 ± 5.3	40.1 ± 3.6	36.6 ± 4.9
	B′	4.9 ± 0.7	5.7 ± 0.6	5.8 ± 1.0
Vinet EOS	*B*	41.9 ± 4.5	39.2 ± 3.1	35.9 ± 4.2
	B′	5.5 ± 0.6	6.1 ± 0.5	6.1 ± 0.8
Method/Material		$\mathbf{MoS_2/MoSe_2}$	$\mathbf{MoS_2/WS_2}$	$\mathbf{MoS_2/WSe_2}$
Murnaghan EOS	*B*	38.4 ± 5.1	38.6 ± 3.6	39.2 ± 4.2
	B′	5.2 ± 0.7	5.3 ± 0.5	5.2 ± 0.6
Birch−Murnaghan EOS	*B*	40.5 ± 4.9	38.4 ± 2.8	39.5 ± 4.2
	B′	5.6 ± 0.8	6.1 ± 0.5	5.7 ± 0.7
Vinet EOS	*B*	39.4 ± 4.1	37.6 ± 2.2	38.5 ± 3.5
	B′	6.0 ± 0.6	6.4 ± 0.4	6.1 ± 0.5

Method/Material		**$MoSe_2/WS_2$**	**$MoSe_2/WSe_2$**	**WS_2/WSe_2**
Murnaghan EOS	B	33.8 ± 4.1	38.2 ± 4.3	34.3 ± 6.8
	B'	5.8 ± 0.8	4.8 ± 0.6	5.7 ± 1.3
Birch−Murnaghan EOS	B	33.7 ± 4.0	39.8 ± 4.2	36.2 ± 6.8
	B'	6.7 ± 1.1	5.3 ± 0.7	6.1 ± 1.6
Vinet EOS	B	33.6 ± 3.3	38.5 ± 3.5	35.8 ± 5.9
	B'	6.8 ± 0.7	5.8 ± 0.5	6.4 ± 1.2

7. Phonon Spectra for Additional Junctions

In this section, we provide additional phonon spectra not presented in the main text. **Figure S13** presents the phonon spectra of several homogeneous and alternating heterogeneous bulk materials, as calculated using both ILP and Lennard-Jones (LJ) potentials, where the universal force field (UFF) parameters are adopted for the latter.[10] Notably, the isotropic LJ potential yields considerably lower out-of-plane phonon energies compared to those obtained using the ILP. **Figure S14** presents the phonon dispersion curves of the three bilayer homojunctions and the six bilayer heterojunctions calculated using the ILP and the LJ potential with the Stillinger-Weber (SW) intralayer potential.[11]

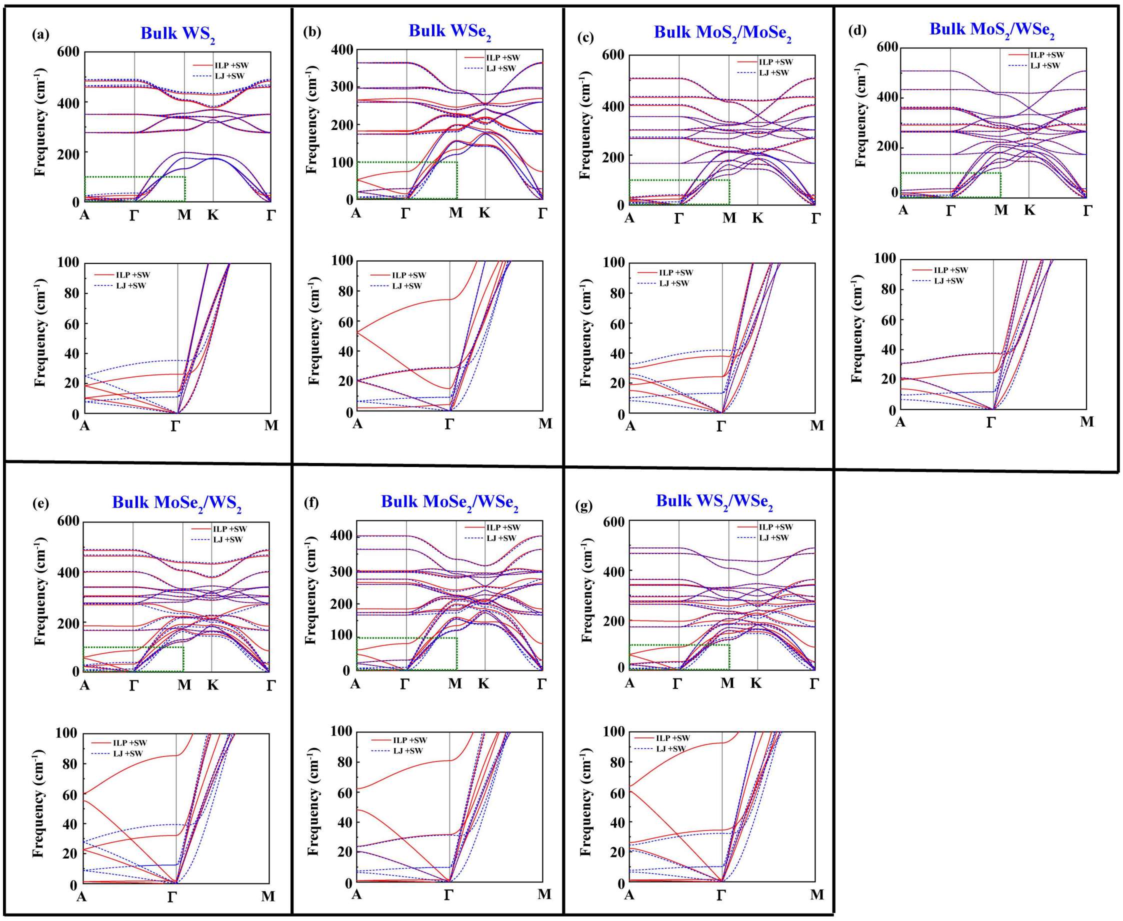

Figure S13. Phonon spectra calculated using ILP (red lines) and LJ (dashed blue lines) potentials with the SW intralayer potential[11] for additional bulk homo- (a,b) and heterojunctions (c-g). The green rectangles (around the Γ-point) in the top subpanels denote a zoomed-in area, shown in the lower subpanels, focusing on the low-energy phonon modes.

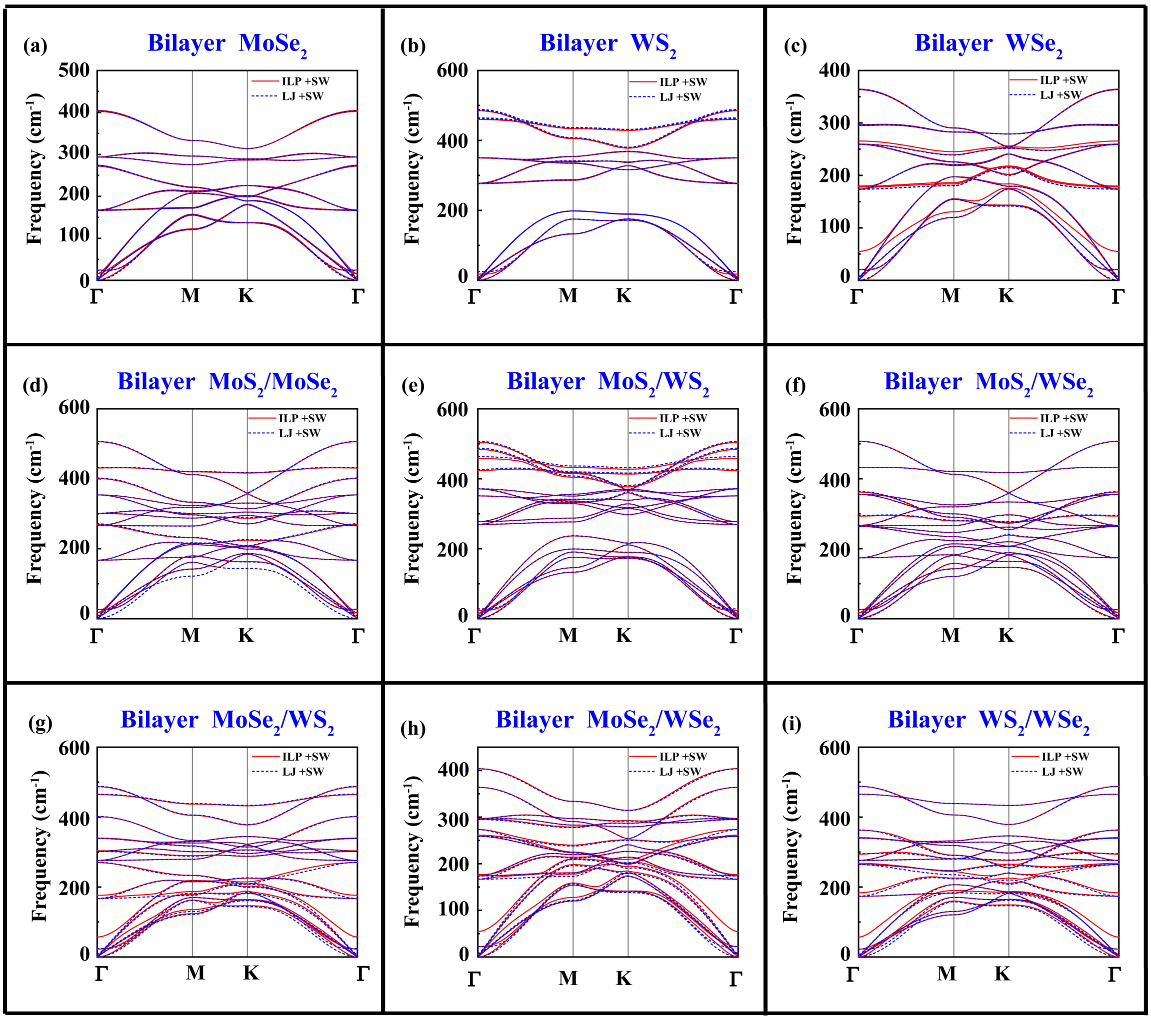

Figure S14. Phonon spectra calculated using the ILP (red lines) and the LJ potential (dashed blue lines) with the SW intralayer potential[11] for bilayer homo- (a-c) and heterojunctions (d-i).

In the above calculations, the supercells used for the bulk and bilayer configurations contain 25×25×6 (a total of 45,000 atoms) and 25×25×1 (a total of 7,500 atoms) unit cells, respectively. In both cases, 201 reciprocal space k-points were used to calculate and plot each branch of the phonon spectrum. We note that the choice of interlayer potential affects mostly the low energy phonon dispersion (around the *Γ*-point) that corresponds to the interlayer phonon modes.

References

(1) Ouyang, W.; Sofer, R.; Gao, X.; Hermann, J.; Tkatchenko, A.; Kronik, L.; Urbakh, M.; Hod, O., Anisotropic Interlayer Force Field for Transition Metal Dichalcogenides: The Case of Molybdenum Disulfide. *J. Chem. Theory Comput.* **2021,** *17* (11), 7237-7245.

(2) Plimpton, S., Fast Parallel Algorithms for Short-Range Molecular Dynamics. *J. Comput. Phys.* **1995,** *117* (1), 1-19.

(3) Ouyang, W.; Azuri, I.; Mandelli, D.; Tkatchenko, A.; Kronik, L.; Urbakh, M.; Hod, O., Mechanical and Tribological Properties of Layered Materials under High Pressure: Assessing the Importance of Many-Body Dispersion Effects. *J. Chem. Theory Comput.* **2020,** *16*, 666.

(4) Hanfland, M.; Beister, H.; Syassen, K., Graphite under pressure: Equation of state and first-order Raman modes. *Phys. Rev. B* **1989,** *39* (17), 12598-12603.

(5) Murnaghan, F. D., The Compressibility of Media under Extreme Pressures. *Proc. Natl. Acad. Sci. U.S.A.* **1944,** *30* (9), 244-247.

(6) Birch, F., Finite Elastic Strain of Cubic Crystals. *Phys. Rev.* **1947,** *71* (11), 809-824.

(7) Birch, F., Elasticity and constitution of the Earth's interior. *J. Geophys. Res.* **1952,** *57* (2), 227-286.

(8) Vinet, P.; Smith, J. R.; Ferrante, J.; Rose, J. H., Temperature effects on the universal equation of state of solids. *Phys. Rev. B* **1987,** *35* (4), 1945-1953.

(9) Vinet, P.; Ferrante, J.; Smith, J. R.; Rose, J. H., A universal equation of state for solids. *J. Phys. C: Solid State Phys.* **1986,** *19* (20), L467.

(10) Rappe, A. K.; Casewit, C. J.; Colwell, K. S.; Goddard, W. A., III; Skiff, W. M., UFF, a full periodic table force field for molecular mechanics and molecular dynamics simulations. *J. Am. Chem. Soc.* **1992,** *114* (25), 10024-10035.

(11) Jiang, J.-W., Misfit Strain-Induced Buckling for Transition-Metal Dichalcogenide Lateral Heterostructures: A Molecular Dynamics Study. *Acta Mech. Solida Sin.* **2019,** *32* (1), 17-28.